INVERSE CONSISTENT DEFORMABLE IMAGE REGISTRATION

YUNMEI CHEN AND XIAOJING YE

Department of Mathematics, University of Florida, Gainesville, FL 32611, USA

Dedicated to the memory of Professor Alladi Ramakrishnan

Abstract. This paper presents a novel variational model for inverse consistent deformable image registration. The proposed model deforms both source and target images simultaneously, and aligns the deformed images in the way that the forward and backward transformations are inverse consistent. To avoid the direct computation of the inverse transformation fields, our model estimates two more vector fields by minimizing their invertibility error using the deformation fields. Moreover, to improve the robustness of the model to the choice of parameters, the dissimilarity measure in the energy functional is derived using the likelihood estimation. The experimental results on clinical data indicate the efficiency of the proposed method with improved robustness, accuracy and inverse consistency.

1. Introduction

Image registration is a very important subject that has been widely applied in medical research and clinical applications. The task of image registration is to find a transformation field that relates points in the source image to their corresponding points in the target image. Deformable image registration allows localized transformations, and is able to account for internal organ deformations. Therefore, it has been increasingly used in health care to assist diagnosis and treatments. In particular, deformable image registration has become a critical technique for image guided radiation therapy. It allows more precise tumor targeting and normal tissue preservation. A comprehensive review of image registration in radiation therapy can be found in [Kes06].

A deformable image registration is called inverse consistent, if the correspondence between two images is invariant to the order of the choice of source and target. More precisely, let S and T be the source and target images, and h and g be the forward and backward transformations, respectively, i.e.

$$S \circ h = T \text{ and } T \circ g = S,$$

then an inverse consistent registration satisfies $h \circ g = id$ and $g \circ h = id$, where id is the identity map. This can be illustrated by the following diagram with constraints

1991 *Mathematics Subject Classification.* Primary 62H35; Secondary 65K10.

Key words and phrases. image registration, inverse consistent, variational method, optimization.

$g = h^{-1}, h = g^{-1}$:

$$\boxed{S} \underset{g}{\overset{h}{\rightleftarrows}} \boxed{T}\,, \tag{1}$$

where each of the two squares in (1) represents the domain on which the labeled image is defined. By applying an inverse consistent registration, measurements or segmentations on one image can be precisely transferred to the other. In imaging guided radiation therapy, the inverse consistent deformable registration technique provides the voxel-to-voxel mapping between the reference phase and the test phase in four-dimensional (4D) radiotherapy [LOC+06]. This technique is referred to "automatic re-contouring".

Inverse consistent deformable image registration has been an active subject of study in the literature. There has been a group of work developed in the context of large deformation by diffeomorphic metric mapping, e.g. [HC03, JDJG04, AGG06, BK07]. The main idea of this method is modeling the forward and backward transformations as a one-parameter diffeomorphism group. Then, a geodesic path connecting two images is obtained by minimizing an energy functional symmetric to the forward and backward transformations. This type of models produce a very good registration results. However, it take long time to compute, since strong regularization of the mappings are required.

Variational method is one of the popular approaches for inverse consistent deformable image registration. This method minimizes an energy functional(s) symmetric to the forward and backward transformations, and in general, consists of three parts: regularization of deformation fields, dissimilarity measure of the target and deformed source images, and penalty of inverse inconsistency [CJ01, ADPS02, RK06, ZJT06]. In [CJ01], Christensen and Johnson proposed to minimize the following coupled energy functionals with respect to h and g alternately:

$$\begin{cases} E(h) = & \lambda E_s(S \circ h, T) + E_r(u) + \rho \|h - g^{-1}\|^2_{L^2(\Omega)} \\ E(g) = & \lambda E_s(T \circ g, S) + E_r(v) + \rho \|g - h^{-1}\|^2_{L^2(\Omega)} \end{cases}, \tag{2}$$

where u and v are forward and backward deformation fields corresponding to h and g, respectively, i.e. $h(x) = x + u(x)$ and $g(x) = x + v(x)$. The dissimilarity measure E_s and the regularization of the deformation field E_r are defined by

$$E_s(S \circ h, T) = \|S \circ h - T\|^2_{L^2(\Omega)}, \quad E_r(u) = \|a\Delta u + b\nabla(\operatorname{div} u) - cu\|^2_{L^2(\Omega)}$$

with positive constants $a, b, c > 0$. The last term in both energy functionals enforces the inverse consistency of h and g. The solution (u, v) to (2) is obtained by iteratively solving a system of two evolution equations associated with their Euler-Lagrange (EL) equations. This model gives considerably good results with parameters chosen carefully. However, it needs to compute the inverse mappings g^{-1} and h^{-1} explicitly in each iteration, which is computationally intensive can cause cumulated numerical errors in the estimation of inverse mappings.

The variational models developed in [ADPS02] and [ZJT06] have the same framework as in [CJ01], but with different representations of E_s, E_r, and inverse consistent constraints. In [ADPS02] and [ZJT06] the terms $\|h \circ g(x) - x\|^2_{L^2(\Omega)}$ and $\|g \circ h(x) - x\|^2_{L^2(\Omega)}$ are used in the energy functional to enforce the inverse consistency. By using these terms the explicit computation of the inverse transforms of h and g can be avoided during the process of finding optimal forward

and backward transformations. The similarity measure in [ZJT06] is mutual information for multi-modal image registration. The $E_s(S \circ h, T)$ in [ADPS02] is $\|S \circ h - T\|^2_{L^2(\Omega)} / \max |DT|$. The regularization term $E_r(u)$ in [ZJT06] is a function of Du, and that in [ADPS02] is a tensor based smoothing which is designed to prevent the transformation fields from being smoothed across the boundaries of features. In [YS05, YTS$^+$08] the proposed models incorporated stochastic errors in the inverse consistent constraints for both forward and backward transformations.

In [LHG$^+$05], Leow *et al.* proposed a non-variational approach that updates the forward and backward transformations simultaneously by a force that reduces the first two terms in $E(h)$ and $E(g)$ in (2) and preserves the inverse consistency. However, in order to simplify the computation this algorithm only takes linear order terms in the Taylor expression to approximate the inverse consistent conditions for updated transformation fields. As a consequence, the truncating errors can be accumulated and exaggerated during iterations. This can lead to large inverse consistent error, despite that it can produce a good matching quickly [ZC08].

In this paper we propose a novel variational model to improve the accuracy, robustness and efficiency of inverse consistent deformable registration. As an alternate to the current framework of variational methods which finds the forward and backward transformations that deform a source image S to match a target image T and vice versa, we propose to deform S and T simultaneously, and let the registration align the deformed source and deformed target images. It is clear that the disparity between deformed S and deformed T is smaller than that between deformed S and fixed T or deformed T and fixed S. Therefore, the deformation by the bidirectional simultaneous deformations is in general smaller than the deformation by unidirectional deformation that deforms S full way to T or T full way to S. As shown in section 5, deforming S and T simultaneously leads to a faster and better alignment than deforming S to the fixed T or vice versa. Let ϕ and $\tilde{\phi}$ represent the transformation fields such that $S \circ \phi$ matches $T \circ \tilde{\phi}$. It is not difficult to verify that if ϕ and $\tilde{\phi}$ are invertible, then the registrations from S to T, and T to S are inverse consistent. To avoid the direct computation of the inverse transformations of ϕ and $\tilde{\phi}$, our model seeks for two additional deformation fields ψ, $\tilde{\psi}$ such that ϕ and ψ are inverse to each other, and the same for $\tilde{\phi}$ and $\tilde{\psi}$. Moreover, the registration process enforces certain regularization of these four deformation fields, and aligns the deformed S and deformed T. Then, the optimal inverse consistent transformations from S to T, and T to S can be obtained simply by appropriate compositions of these four transformations.

The idea of deforming S and T simultaneously has been adopted in the models where the forward or backward transformation is modeled as a one-parameter diffeomorphism group [AGG06]. However, our model finds regularized invertible deformation fields by minimizing the L^2 norms of the deformation fields and inverse consistent errors rather than a one-parameter diffeomorphism group, whose computational cost is very expensive and hence hinders its application in clinical use. Moreover, our model allows parallel computations for all the deformation fields to significantly reduce the computational time.

Furthermore, to improve the robustness of the model to noises and the choice of the parameter λ that balances the goodness of matching and smoothness of the deformation fields (see the λ in $E(h)$ and $E(g)$ of (2)), we adopt the maximum likelihood estimate (MLE) that is able to accommodate certain degree of variability

in matching to improve the robustness and accuracy of the registration. By using MLE, the ratio of weighting parameters on the sum of squared distance (SSD) of the residue image $S \circ \phi - T \circ \tilde{\phi}$ and the regularization term is not a fixed λ, but λ/σ^2 (see (18) below). This results in a self-adjustable weighting factor that makes the choice of λ more flexible, and also speeds up the convergence to the optimal deformation field.

The rest of the paper is organized as follows. In section 2, we present a detailed description of the proposed model. The existence of solutions to the proposed model is shown in section 3. The calculus of variation and an outline of a fast algorithm for solving the proposed model numerically are provided in section 4. In section 5, we present the experimental results on clinical data, and the application in auto re-contouring. The last section concludes the paper.

2. Proposed Method

Let S and T be the source and target images defined on Ω_S and Ω_T in $\mathbb{R}^d$, respectively. Note that, in real applications, Ω_S and Ω_T are usually fully overlapped. For simplicity we assume that images S and T are real-valued functions with continuous derivatives. Let $|\cdot|$ denote the absolute value (length) of a scaler (vector) in Euclidean spaces, and $\|\cdot\|$ denote $\|\cdot\|_{L^2(\Omega)}$ henceforth. We also extend this notation to vector-valued functions whose components are in L^2 or H^1: $u = (u_1, \cdots, u_d)^\top$ with each component $u_j \in H^1(\Omega)$, $j = 1, \cdots, d$, there is

$$\|u\|_{H^1(\Omega)} \triangleq \left(\|u\|^2 + \|Du\|^2\right)^{1/2}$$

and

$$\|u\| \triangleq \left(\sum_{j=1}^{d} \|u_j\|^2\right)^{1/2}, \quad \|Du\| \triangleq \left(\sum_{j=1}^{d} \|Du_j\|^2\right)^{1/2},$$

where

$$\|u_j\| = \left(\int_\Omega |u_j(x)|^2 dx\right)^{1/2} \quad \text{and} \quad \|Du_j\| = \left(\int_\Omega |Du_j(x)|^2 dx\right)^{1/2},$$

for $j = 1, \cdots, d$.

2.1. Motivation and Ideas of Proposed Method.

In this paper, we propose a novel variational model for inverse consistent deformable registration to improve its efficiency and robustness. Our idea differs from the current framework which deforms source image S to target image T, or vice versa: as an alternate, we propose to deform S and T simultaneously, and match both deformed images. This means that ideally we pursuit for a pair of half-way transforms $\phi : \Omega_S \to \Omega_M$ and $\tilde{\phi} : \Omega_T \to \Omega_M$ such that $S \circ \phi = T \circ \tilde{\phi}$, where Ω_M is the region where $S \circ \phi$ and $T \circ \tilde{\phi}$ have overlap. To ensure the transformations from S to T and T to S are inverse consistent, the transforms ϕ and $\tilde{\phi}$ are required to be invertible (but not necessarily to be inverse to each other). Hence, our purpose is to find the transformations ϕ and $\tilde{\phi}$ such that

$$S \circ \phi = T \circ \tilde{\phi}, \quad \phi, \tilde{\phi} \text{ invertible.} \tag{3}$$

To avoid direct computation of inverses of ϕ and $\tilde{\phi}$ during iterations, we enforce the invertibility of ϕ and $\tilde{\phi}$ by finding another two transformations $\psi : \Omega_M \to \Omega_S$

and $\tilde{\psi} : \Omega_M \to \Omega_T$ such that

$$\begin{aligned} \psi \circ \phi = id, \qquad & \phi \circ \psi = id, \\ \tilde{\psi} \circ \tilde{\phi} = id, \qquad & \tilde{\phi} \circ \tilde{\psi} = id. \end{aligned} \tag{4}$$

Once we obtained such ψ and $\tilde{\psi}$, we can construct the objective full-way transformations h and g as follows,

$$h = \phi \circ \tilde{\psi}, \quad g = \tilde{\phi} \circ \psi.$$

It is easy to see that h and g satisfy the inverse consistent constraints $h \circ g = g \circ h = id$. This idea is illustrated by the following diagram, where M is an intermediate image.

(5)

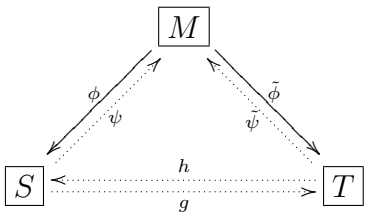

Since by deforming S and T simultaneously the difference between deformed S and deformed T at each iteration, in general, is smaller than that between deformed S and fixed T, or deformed T and fixed S, the computational cost of deforming both S and T is much less than the conventional one that deform S all the way to T and T to S. In particular, if the underlying deformations of h and g are large, deforming both S and T can make the each deformation of ϕ and $\tilde{\phi}$ in the proposed model almost half smaller than that of h and g, and achieve a faster convergence for the computation of ϕ and $\tilde{\phi}$. Also, seeking ψ and $\tilde{\psi}$ along with ϕ and $\tilde{\phi}$ avoids direct computation of inverse transformations in each iteration as that in (4), which usually causes cumulated errors during iterations if using approximations of the inverses.

Moreover, regularizing the deformation fields is very important to obtain physically meaningful and accurate registrations. Also, if the energy functional consists of only dissimilarity measures and invertible constraints, it is ill-posed in general. Therefore, we propose the following framework for deformable inverse consistent registration:

$$\min_{\phi,\tilde{\phi},\psi,\tilde{\psi}} R(\phi, \tilde{\phi}, \psi, \tilde{\psi}) + \mathrm{dis}(S \circ \phi, T \circ \tilde{\phi}), \quad \text{s.t. condition (4) holds} \tag{6}$$

where R is a regularization operator of its arguments, $\mathrm{dis}(S \circ \phi, T \circ \tilde{\phi})$ measures the dissimilarity between $S \circ \phi$ and $T \circ \tilde{\phi}$.

2.2. **Alternative Formulation of (4) Using Deformation Fields.** Let the functions u, $\tilde{u}$, v and $\tilde{v}$ represent the corresponding deformation fields of the transformations ϕ, $\tilde{\phi}$, ψ and $\tilde{\psi}$, respectively. That is,

$$\begin{aligned} \phi(x) = x + u(x), \quad & \tilde{\phi}(x) = x + \tilde{u}(x), \\ \psi(x) = x + v(x), \quad & \tilde{\psi}(x) = x + \tilde{v}(x). \end{aligned} \tag{7}$$

Then, the constraints in (4) can be rewritten as

$$u + v(x+u) = v + u(x+v) = 0, \tag{8}$$
$$\tilde{u} + \tilde{v}(x+\tilde{u}) = \tilde{v} + \tilde{u}(x+\tilde{v}) = 0.$$

2.3. **MLE based derivation for** $\mathrm{dis}(S\circ\phi, T\circ\tilde{\phi})$**.** To improve the robustness of the algorithm for deformable image registration, we use the negative log-likelihood of the residue image as a measure of mismatching. Consider voxel intensities of the residue image defined by

$$W(x) \triangleq S\circ\phi(x) - T\circ\tilde{\phi}(x), \quad x\in\Omega_M,$$

as independent samples drawn from a Gaussian distribution of mean zero and variance σ^2 to be optimized (see remark below for the reason of this assumption), whose probability density function (pdf) is denoted by $P(\cdot|\sigma)$. Then the likelihood of the residual image $W(x)$ can be computed as

$$\mathcal{L}(\sigma|\{W(x), x\in\Omega\}) = \prod_{x\in\Omega} P(W(x)|\sigma) = \prod_{x\in\Omega}\left(\frac{1}{\sqrt{2\pi}\sigma}e^{-|S\circ\phi - T\circ\tilde{\phi}|^2/2\sigma^2}\right). \tag{9}$$

Then, by writing the summation over all $x\in\Omega$ as an integral over Ω the negative log-likelihood function is given as follows:

$$\|S\circ\phi - T\circ\tilde{\phi}\|^2/2\sigma^2 + |\Omega|\log\sqrt{2\pi}\sigma.$$

Omitting the constant $\Omega\log\sqrt{2\pi}$, we define the dissimilarity term as

$$\mathrm{dis}(S\circ\phi, T\circ\tilde{\phi}) \triangleq \|S\circ\phi - T\circ\tilde{\phi}\|^2/2\sigma^2 + |\Omega|\log\sigma. \tag{10}$$

which can be rewritten as our MLE fitting term F by using corresponding deformation fields u and $\tilde{u}$:

$$F(u,\tilde{u},\sigma) \triangleq \mathrm{dis}(S(x+u), T(x+\tilde{u})) = \|S(x+u) - T(x+\tilde{u})\|^2/2\sigma^2 + |\Omega|\log\sigma. \tag{11}$$

Remark 2.1. Let $\hat{P}$ be the estimation of the pdf for the random variable $X \triangleq W(x)$, $x\in\Omega$. We show below why it is reasonable to assume $\hat{P}$ to be a Gaussian distribution of zero mean and variance σ^2.

In fact, $\hat{P}$ is a function in $C_0(\mathbb{R})$, the space of all the continuous functions on real line vanishing at infinity with the supreme norm. Let $H_0(\mathbb{R})$ be the Hilbert space consisting of all linear combinations of $\kappa(x_l, x)$ for finite many of $x_l\in\mathbb{R}$, where

$$\kappa(x_l, x) = \left(2\pi\sigma^2\right)^{-1/2} e^{-(x_l - x)^2/2\sigma^2}, \quad \forall\, x\in\mathbb{R}. \tag{12}$$

Define an inner product on $H_0(\mathbb{R})$ by

$$\left\langle \sum_{i=1}^m a_i\kappa(x_i,\cdot), \sum_{j=1}^n b_j\kappa(y_j,\cdot)\right\rangle_{H_0(\mathbb{R})} = \sum_{i=1}^m\sum_{j=1}^n a_i b_j \kappa(x_i, y_j).$$

We claim that

$$H_0(\mathbb{R}) \text{ is dense in } C_0(\mathbb{R}). \tag{13}$$

In fact, if the claim (13) is not true, by Hahn-Banach theorem there exists a bounded signed measure $\mathfrak{m}$ in the dual space of $C_0(\mathbb{R})$, such that

$$\int_{\mathbb{R}} \hat{P}\, d\mathfrak{m} \neq 0, \tag{14}$$

but $\int_{\mathbb{R}} f d\mathfrak{m} = 0$, for all $f \in H_0(\mathbb{R})$. In particular, for any $x \in \mathbb{R}$,

$$\int_{\mathbb{R}} \kappa(x, y) d\mathfrak{m}_y = 0,$$

where $\kappa(\cdot, \cdot)$ is as in (12), and hence,

$$\int_{\mathbb{R}\times\mathbb{R}} \kappa(x, y) d\mathfrak{m}_x d\mathfrak{m}_y = 0.$$

This implies $\mathfrak{m} = 0$, which contradicts (14). Therefore, the claim holds.

By this claim it is easy to see that

$$\hat{P}(z) \approx \sum_{l=1}^{k} \alpha_l \kappa(x_l, z) = \left(2\pi\sigma^2\right)^{-1/2} \sum_{l=1}^{k} \alpha_l e^{-(x_l - z)^2/2\sigma^2} \tag{15}$$

for some $\{x_l; \alpha_l\}_{l=1}^k$. Since a good registration requires the the intensities of the residue image $W(x)$ close to zero. Hence, in (15) the only dominate term in the sum should be the one corresponding to $x_l = 0$, and other terms are negligible. This means that $\hat{P}$ is approximately $\mathcal{N}(0, \sigma^2)$, the Gaussian distribution with mean 0 and variance σ^2.

2.4. **Proposed model.** Base on the discussion above, we are ready to present the proposed model. We define the regularization term $R(\phi, \tilde{\phi}, \psi, \tilde{\psi})$ in (6) using their corresponding deformation fields as

$$R(\phi, \tilde{\phi}, \psi, \tilde{\psi}) = R(u, \tilde{u}, v, \tilde{v}) \triangleq \|Du\|^2 + \|D\tilde{u}\|^2 + \|Dv\|^2 + \|D\tilde{v}\|^2. \tag{16}$$

By plugging (16) and (11) into (6), and replacing the constraint in (6) by (8), the proposed model can be written as:

$$\min_{u,\tilde{u},v,\tilde{v},\sigma} R(u, \tilde{u}, v, \tilde{v}) + \lambda F(u, \tilde{u}, \sigma), \quad \text{s.t. condition (8) holds}, \tag{17}$$

where $R(u, \tilde{u}, v, \tilde{v})$ and $F(u, \tilde{u}, \sigma)$ are defined in (16) and (11), respectively.

To solve problem (17), we relax the equality constraints of inverse consistency, and penalize their violation using quadratic functions, then write it as an unconstrained energy minimization problem

$$\min_{u,\tilde{u},v,\tilde{v},\sigma} R(u, \tilde{u}, v, \tilde{v}) + \lambda F(u, \tilde{u}, \sigma) + \mu \left(\mathcal{I}(u, v) + \mathcal{I}(\tilde{u}, \tilde{v})\right), \tag{18}$$

where and $\mathcal{I}(u, v)$ is the cost of inverse inconsistency of u and v:

$$\mathcal{I}(u, v) = \mathcal{I}_v(u) + \mathcal{I}_u(v), \tag{19}$$

with

$$\mathcal{I}_v(u) = \|u + v(x + u)\|^2 \quad \text{and} \quad \mathcal{I}_u(v) = \|v + u(x + v)\|^2. \tag{20}$$

Similarly, we have $\mathcal{I}(\tilde{u}, \tilde{v})$. With sufficiently large μ, solving (18) gives an approximation to the solution of (17).

The term $F(u, \tilde{u}, \sigma)$ is from the negative log-likelihood of the residual image (11). Minimizing this term forces the mean of the residue image to be zero, but allows it to have a variance to accommodate certain variability. This makes the model more robust to noise and artifacts, and less sensitive to the choice of the parameter λ than the model using the SSD, i.e. the squared L^2-norm, of the residue image as a dissimilarity measure as in (2). The parameter λ balances the smoothness of deformation fields and goodness of alignments, and affects the registration result significantly. In the proposed model, the ratio of the SSD of the residue image

over the smoothing terms is λ/σ^2 rather than a prescribed λ. Since σ is to be optimized, and from its EL equation σ is the standard deviation of the residue image. Therefore, in the proposed model the weight on the matching term updates during iterations. When the alignment gets better, σ the standard deviation of the residue as shown in (35) decreases, and hence the weight on the matching term automatically increases. This self-adjustable feature of the weight not only enhances the accuracy of alignment, but also makes the choice of λ flexible, and results in a fast convergence.

As shown earlier, the final forward and backward transforms h and g can be obtained by

$$h = \phi \circ \tilde{\psi} = x + \tilde{v} + u(x + \tilde{v}) \quad \text{and} \quad g = \tilde{\phi} \circ \psi = x + \tilde{u} + v(x + \tilde{u}).$$

Thus, the corresponding final full-way forward and backward deformation fields $\bar{u}$ and $\bar{v}$ are given as

$$\bar{u} = \tilde{v} + u(x + \tilde{v}) \quad \text{and} \quad \bar{v} = \tilde{u} + v(x + \tilde{u}), \tag{21}$$

respectively. Then the inverse consistent constraints (4) can be represented using $\bar{u}, \bar{v}$ as follows:

$$\bar{u} + \bar{v}(x + \bar{u}) = \bar{v} + \bar{u}(x + \bar{v}) = 0. \tag{22}$$

3. Existence of Solutions

In this section we prove the existence of solutions $(u, \tilde{u}, v, \tilde{v}, \sigma)$ to the proposed model (18). For simplicity, we assume that both S and T defined on the same domain Ω, which is simply connected, closed and bounded in $\mathbb{R}^d$ with Lipschitz boundary $\partial\Omega$. Also $S, T \in C^1(\Omega)$. As in reality, deformation field cannot be unbounded, we restrict $u, \tilde{u}, v, \tilde{v}$ to be in a closed subset of $L^\infty(\Omega)$:

$$\mathcal{B} \triangleq \left\{ u \in L^\infty(\Omega) : \|u\|_{L^\infty(\Omega)} \leq B,\ B \in \mathbb{R}_+ \text{ only depends on } \Omega \right\}$$

Then, we seek solutions $(u, \tilde{u}, v, \tilde{v}, \sigma)$ to the problem (18) in the spaces $u, \tilde{u}, v, \tilde{v} \in H^1(\Omega) \cap \mathcal{B}$ and $\sigma \in \mathbb{R}_+$. For short notations, we let w denote the quaternion $(u, \tilde{u}, v, \tilde{v})$. Then, we show the existence of solutions to the following minimization problem:

$$\min_{(w,\sigma) \in (H^1 \cap \mathcal{B}) \times \mathbb{R}_+} E(w, \sigma) \tag{23}$$

where

$$E(w, \sigma) = \|Dw\|^2 + \lambda F(w, \sigma) + \mu \mathcal{I}(w)$$

and F and $\mathcal{I}$ are defined correspondingly in (18) using the simplified notation of w, i.e.

$$\begin{aligned} \|Dw\|^2 &= \|Du\|^2 + \|D\tilde{u}\|^2 + \|Dv\|^2 + \|D\tilde{v}\|^2, \\ F(w, \sigma) &= \|S(x + u) - T(x + \tilde{u})\|^2/\sigma^2 + |\Omega| \log \sigma, \\ \mathcal{I}(w) &= \mathcal{I}_v(u) + \mathcal{I}_u(v) + \mathcal{I}_{\tilde{v}}(\tilde{u}) + \mathcal{I}_{\tilde{u}}(\tilde{v}). \end{aligned}$$

and the terms on the right side of $\mathcal{I}(w)$ are defined as in (20). The λ and μ are prescribed positive constants.

Theorem 3.1. *The minimization problem (23) admits solutions* $(w, \sigma) \in \left(H^1 \cap \mathcal{B}\right) \times \mathbb{R}_+$.

Proof. For $(w,\sigma) \in \left(H^1 \cap \mathcal{B}\right) \times \mathbb{R}_+$, $E(w,\sigma)$ is bounded below. Hence, there exists a minimizing sequence $\{(w_k,\sigma_k)\}_{k=1}^{\infty} \subset \left(H^1 \cap \mathcal{B}\right) \times \mathbb{R}_+$ such that

$$\lim_{k\to\infty} E(w_k,\sigma_k) = \inf_{(H^1\cap\mathcal{B})\times\mathbb{R}_+} E(w,\sigma).$$

Therefore $\{\|Dw_k\|\}_{k=1}^{\infty}$ are uniformly bounded. Along with $w_k \in \mathcal{B}$ we know that $\{w_k\}_{k=1}^{\infty}$ is a bounded sequence in H^1. By the weak compactness of H^1 and the fact that H^1 is precompact in L^2, there exists a convergent subsequence, which is still denoted by $\{w_k\}_{k=1}^{\infty}$, and a function $\hat{w} \in H^1$, such that

$$w_k \rightharpoonup \hat{w} \quad \text{weakly in } H^1, \tag{24}$$

$$w_k \to \hat{w} \quad \text{strongly in } L^2, \text{ and a.e. in } \Omega. \tag{25}$$

Moreover, since $E(w_k,\sigma_k) \to \infty$ if $\sigma_k \to 0$ or ∞, there is a constant $C > 0$ such that $\{\sigma_k\}_{k=1}^{\infty}$ are bounded below and above by $1/C$ and C respectively. Hence, there is a subsequence of $\{\sigma_k\}_{k=1}^{\infty}$ and a scaler $\hat{\sigma} \in \mathbb{R}_+$, without changing the notation for the subsequence we have

$$\sigma_k \to \hat{\sigma} \in \mathbb{R}_+. \tag{26}$$

From the weak lower semi-continuity of norms and (24), we know

$$\|D\hat{w}\|^2 \le \lim_{k\to\infty} \|Dw_k\|^2. \tag{27}$$

Also, as $\mathcal{I}(w) \le 8B$ for any $w \in H^1 \cap \mathcal{B}$ and $w_k \to \hat{w}$ a.e. in Ω, we get, by dominant convergence theorem, that

$$\lim_{k\to\infty} \mathcal{I}(w_k) = \mathcal{I}(\hat{w}). \tag{28}$$

By the same argument with the smoothness of S and T, the convergence of $\{\sigma_k\}_{k=1}^{\infty}$, and the fact that $w_k \to \hat{w}$ a.e. in Ω, we can also have

$$\lim_{k\to\infty} F(w_k,\sigma_k) = F(\hat{w},\hat{\sigma}) \tag{29}$$

Combining (27), (28) with (29), we obtain that

$$E(\hat{w},\hat{\sigma}) \le \lim_{k\to\infty} E(w_k,\sigma_k) = \inf_{(H^1\cap\mathcal{B})\times\mathbb{R}_+} E(w,\sigma).$$

Furthermore, since $\{w_k\}_{k=1}^{\infty} \subset \mathcal{B} \subset L^\infty(\Omega)$, we know

$$w_k \overset{\text{W}*}{\rightharpoonup} \hat{w} \quad \text{weakly* in } L^\infty$$

and hence $\hat{w} \in \mathcal{B}$. Therefore, $(\hat{w},\hat{\sigma}) \in \left(H^1 \cap \mathcal{B}\right) \times \mathbb{R}_+$. Hence

$$E(\hat{w},\hat{\sigma}) = \inf_{(H^1\cap\mathcal{B})\times\mathbb{R}_+} E(w,\sigma).$$

which implies that $(\hat{w},\hat{\sigma})$ is a solution to the minimization problem (23). □

4. Numerical Scheme

In this section, we provide the numerical scheme for solving (18). Since the compositions in the inverse consistency constraints $\mathcal{I}_u(v)$ and $\mathcal{I}_v(u)$ bring a difficulty in getting an explicit form of the EL equations for the deformation fields and their inverses, in our computation, instead of directly solving (18), we solve the following two coupled minimization problems alternately:

$$\begin{cases} \min\limits_{u,\tilde{u}} E_{v,\tilde{v},\sigma}(u,\tilde{u}) \\ \min\limits_{v,\tilde{v}} E_{u,\tilde{u}}(v,\tilde{v}) \end{cases} \tag{30}$$

where

$$E_{v,\tilde{v},\sigma}(u,\tilde{u},\sigma) = \|Du\|^2 + \|D\tilde{u}\|^2 + \lambda\, F(u,\tilde{u},\sigma) + \mu\left(\mathcal{I}_v(u) + \mathcal{I}_{\tilde{v}}(\tilde{u})\right) \tag{31}$$

and

$$E_{u,\tilde{u}}(v,\tilde{v}) = \|Dv\|^2 + \|D\tilde{v}\|^2 + \mu\left(\mathcal{I}_u(v) + \mathcal{I}_{\tilde{u}}(\tilde{v})\right). \tag{32}$$

By taking first variation with respect to $u, \tilde{u}, v, \tilde{v}$, we get the EL equations:

$$\begin{cases} -\Delta u + \dfrac{\lambda}{\sigma^2} W_{u,\tilde{u}} DS(x+u) + \mu\left\langle I + Dv(x+u), u + v(x+u)\right\rangle = 0 \\ -\Delta v + \mu\left\langle I + Du(x+v), v + u(x+v)\right\rangle = 0 \\ -\Delta \tilde{u} - \dfrac{\lambda}{\sigma^2} W_{u,\tilde{u}} DT(x+\tilde{u}) + \mu\left\langle I + D\tilde{v}(x+\tilde{u}), \tilde{u} + \tilde{v}(x+\tilde{u})\right\rangle = 0 \\ -\Delta \tilde{v} + \mu\left\langle I + D\tilde{u}(x+\tilde{v}), \tilde{v} + \tilde{u}(x+\tilde{v})\right\rangle = 0 \end{cases}, \tag{33}$$

in Ω, with free Neumann boundary conditions for each of them on $\partial\Omega$:

$$\langle Du, n\rangle = \langle D\tilde{u}, n\rangle = \langle Dv, n\rangle = \langle D\tilde{v}, n\rangle = 0, \quad \text{on } \partial\Omega, \tag{34}$$

where $W_{u,\tilde{u}} \triangleq S(x+u) - T(x+\tilde{v})$, I is the identity matrix of size d, and n is the outer normal of $\partial\Omega$. Also, the first variation of σ gives

$$\sigma = \|S(x+u) - T(x+\tilde{u})\|/|\Omega|^{1/2}. \tag{35}$$

The solution to the EL equations (33) can be obtained by finding the stationary solution to the evolution equations associated with the EL equations. In numerical implementation, we use semi-implicit discrete form of the evolution equations. The additive operator splitting (AOS) scheme was applied to solve the problem faster [WtHRV98]. An alternative way of AOS to solve the semi-implicit discrete evolution equation in this case can be obtained by applying discrete cosine transforms (DCT) to diagonalize the Laplace operator with the assumption that the deformation fields have symmetric boundary condition, which is compatible with (34).

In two-dimensional (2D) case, the semi-implicit discrete form of (33) with fixed step sizes τ_u, τ_v for the evolution equations of $u^{(k+1)}$ as

$$\frac{u_{i,j}^{(k+1)} - u_{i,j}^{(k)}}{\tau_u} = \Delta_{i,j} u^{(k+1)} - D_{i,j}\left(\lambda F\left(u^{(k)}, \tilde{u}^{(k)}, \sigma^{(k)}\right) + \mu \mathcal{I}_{v^{(k)}}\left(u^{(k)}\right)\right), \tag{36}$$

and $v^{(k+1)}$ as

$$\frac{v_{i,j}^{(k+1)} - v_{i,j}^{(k)}}{\tau_v} = \Delta_{i,j} v^{(k+1)} - \mu\, D_{i,j} \mathcal{I}_{u^{(k)}}\left(v^{(k)}\right), \tag{37}$$

where $\Delta_{i,j}$ and $D_{i,j}$ represent the discrete Laplacian and gradient operators at the pixel indexed by (i,j), respectively. The 3D case is a simple analogue with one

Algorithm 1 Inverse Consistent Deformable Image Registration (**icDIR**)

Input S, T, and $\tau_u, \tau_v, \lambda, \mu > 0, \epsilon = .5, \delta_c = 1$. Initialize $(u^{(0)}, \tilde{u}^{(0)}, v^{(0)}, \tilde{v}^{(0)}) = 0$, $k = 0$.
while $\delta_c \geq \epsilon$ **do**
  repeat
    {All terms in $(u^{(k+1)}, \tilde{u}^{(k+1)}, v^{(k+1)}, \tilde{v}^{(k+1)})$ can be calculated in parallel}
    Calculate $(u^{(k+1)}, v^{(k+1)})$ using (36) and (37).
    Calculate $(\tilde{u}^{(k+1)}, \tilde{v}^{(k+1)})$ using (36) and (37) with $(u^{(k+1)}, v^{(k+1)})$ replaced by $(\tilde{u}^{(k+1)}, \tilde{v}^{(k+1)})$.
    update $\sigma^{(k+1)}$ by (35).
    $k \leftarrow k + 1$
  until convergence
  return $(u, \tilde{u}, v, \tilde{v})^{\mu}$
  $(u, \tilde{u}, v, \tilde{v}) \leftarrow (u, \tilde{u}, v, \tilde{v})^{\mu}, \mu \leftarrow 2\mu$.
  Compute $\bar{u}$ and $\bar{v}$ using (21) and then δ_c using (38).
end while

more subscript in indices. Similarly, we have the discrete evolution equation for $\tilde{u}$ and $\tilde{v}$ with the two components within each of the three pairs $(u, \tilde{u})$, $(v, \tilde{v})$ and (S, T) switched in (36) and (37). With AOS scheme being applied, the computation for each update of u involves of solving d tridiagonal systems whose computational costs are linear in N, where N is the total number of pixels in S (or T). Also, in each iteration of updating u and v, there needs $2(d+1)$ interpolations with size N. It is important to point out that, in each iteration, the computations of $u, \tilde{u}, v, \tilde{v}$ can be carried out in parallel. We summarize **icDIR** in Algorithm 1, where the maximum inverse consistency error (ICE) δ_c is defined by

$$\delta_c = \max_x \left\{ |\bar{u} + \bar{v}(x + \bar{u})|, |\bar{v} + \bar{u}(x + \bar{v})| \right\}, \tag{38}$$

and $\bar{u}$ and $\bar{v}$ are the final full-way deformation fields shown in (21). That is, it measures the maximum ICE of deformations obtained by quaternion $(u, \tilde{u}, v, \tilde{v})$. The parameter μ in (18) may increase during iterations to ensure smaller ICE. In each inner loop with fixed μ, the computation is terminated when the mean of $CC(S(x + \bar{u}), T)$ and $CC(T(x + \bar{v}), S)$ converges. We set a stopping tolerance $\epsilon = .5$ and terminate the whole computation once δ_c is lower than ϵ, in which case the maximum ICE is less than half of the grid size between two concatenate pixels/voxels and hence the inverse consistency is exactly satisfied with respect to the original resolution of the images.

5. Experimental Results

In this section, we present the experimental results of proposed model using algorithm 1 (**icDIR**). All implementations involved in the experiments were coded in Matlab v7.3 (R2006b), except the Thomas tridiagonal solver, which was coded in C++. We used build-in functions `interp2/interp3` of Matlab with default settings for interpolations. All Computations were performed on a Linux (version 2.6.16) workstation with Intel Core 2 CPU at 1.86GHz and 2GB memory.

We first test the accuracy of registration and auto re-contouring of the proposed algorithm on a clinical data set of 100 2D-prostate MR images. Each image, called

a phase, is a 2D image of dimension 288×192 that focuses on the prostate area. The first phase is used as a source image S, as shown in Fig. 1(a). The boundaries

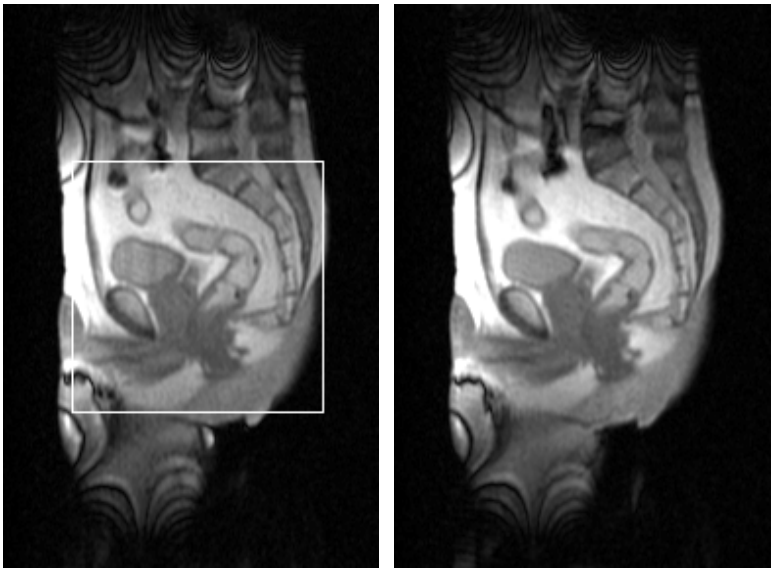

(a) Source image S (b) Target image T

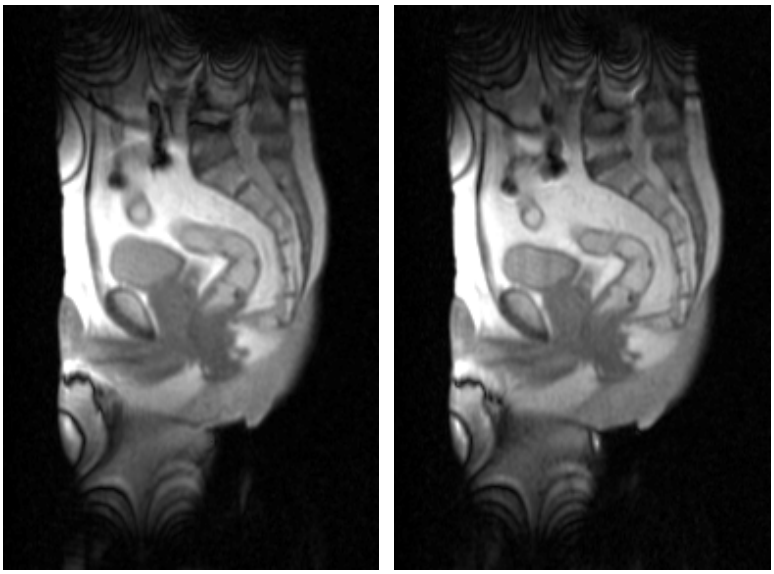

(c) Deformed T (d) Deformed S

FIGURE 1. Inverse consistent registration result by proposed model (18). (a) source image S. (b) target image T. (c) deformed T, i.e. $T(x + \bar{v})$. (d) deformed S, i.e. $S(x + \bar{u})$.

of the regions of interests (ROI) in S were delineated by contours and superimposed

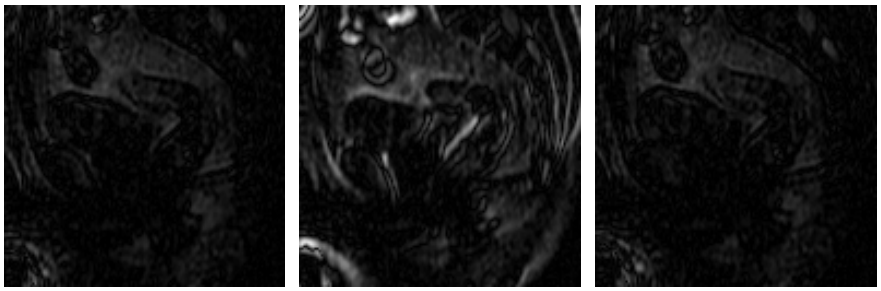

(a) $|S(x+\bar{u})-T|$ (b) $|S-T|$ (c) $|T(x+\bar{v})-S|$

FIGURE 2. Residue image (in the square area shown in Fig. 1(a)) obtained by proposed model (18). (a) $|S(x+\bar{u})-T|$ (b) initial $|S-T|$. (c) $|T(x+\bar{v})-S|$.

by medical experts, as enlarged and shown in Fig. 4(a). The rest 99 phases were considered as targets. In this experiment we applied the proposed model (18) with parameters (λ, μ, τ) set to be $(.05, .2, .05)$ to S and Ts. For demonstration, we only showed the result using the 21st phase as T, as depicted in Fig. 1(b). The deformed T and deformed S, i.e. $T(x+\bar{v})$ and $S(x+\bar{u})$, are shown in the Fig. 1(c) and 1(d) respectively, where $\bar{u}$ and $\bar{v}$ are defined in (21) using the optimal $(u, \tilde{u}, v, \tilde{v})$ obtained by model (18). The errors of the alignments, $|T(x+\bar{v})-S|$ and $|S(x+\bar{u})-T|$, on the squared area (shown in Fig. 1(a)) are displayed in Fig. 2(a) and 2(c), respectively. With comparison to the original error $|S-T|$ shown in Fig. 2(b), we can see the errors of alignments are significantly reduced. This indicates that the proposed registration model (18) has high accuracy in matching two images.

The final optimal forward and backward deformation fields $\bar{u}$ and $\bar{v}$ are displayed by applying them to a domain of regular grids, shown in Fig. 3(a) and 3(c), respectively. Furthermore, to validate the accurate inverse consistency obtained by our model (18), we applied $\bar{u}+\bar{v}(x+\bar{u})$ on a domain with regular grids, and plotted the resulting grids in Fig. 3(b). The resulting grids by $\bar{v}+\bar{u}(x+\bar{v})$ had the same pattern so we omitted it here. From Fig. 3(b), we can see that the resulting grids are the same as the original regular grids. This indicates that the inverse consistent constraints $\bar{u}+\bar{v}(x+\bar{u})=\bar{v}+\bar{u}(x+\bar{v})=0$ are well preserved. We also computed the maximum ICE δ_c using $\bar{u}, \bar{v}$ and (38) and the result was .46. The mean ICE $\left(\|\bar{u}+\bar{v}(x+\bar{u})\|+\|\bar{v}+\bar{u}(x+\bar{v})\|\right)/2|\Omega|$ versus the number of iterations is plotted in Fig. 5, which shows the inverse consistency is preserved during the registration. These imply that the proposed algorithm provides an accurate inverse consistent registration.

An accurate inverse consistent registration can transform segmentations from one image to another accurately. One of the applications is auto re-contouring, that deforms the expert's contours from a planning image to new images during the course of radiation therapy. In this experiment, we had expert's contours superimposed on the source image S as shown in Fig. 4(a). Then by applying the deformation field $\bar{u}$ on this contours we get the deformed contours on the target image T as shown in Fig. 4(b). The accuracy in auto re-contouring is evident.

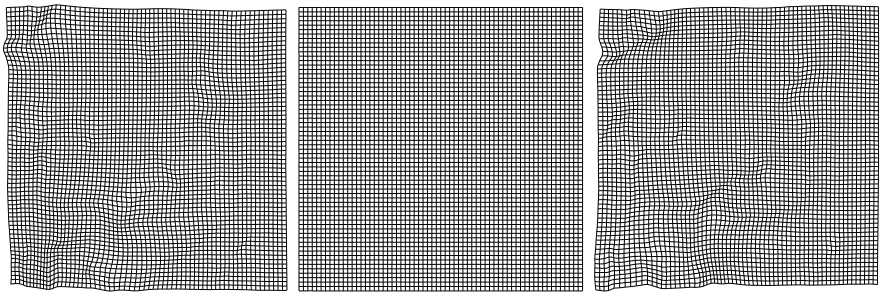

(a) $\bar{u}$ (b) $\bar{u} + \bar{v}(x + \bar{u})$ (c) v

FIGURE 3. Deformation fields obtained by proposed model (18) in the zoomed-in area applied on regular grid with half of original resolution of images. (a) $\bar{u}$. (b) $\bar{u} + \bar{v}(x + \bar{u})$, which demonstrates the inverse consistency is well preserved. (c) $\bar{v}$.

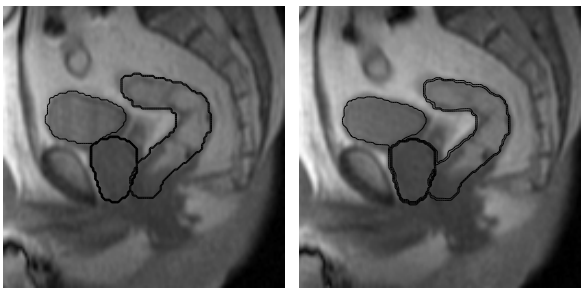

(a) Original Contour on S (b) Re-contouring on T

FIGURE 4. Auto re-contouring result using the deformation field $\bar{u}$ obtained by proposed model (18). Images are zoomed-ins of the square area shown in Fig. 1(a). (a) S with initial contours on ROIs (drawn by medical expert). (b) T with re-contouring on ROIs by applying deformation field $\bar{u}$ to the initial contours.

The second experiment was aimed to test the efficiency of the proposed model (18) in registering 3D images. We applied (18) to a pair of 3D chest CT images of dimension $64 \times 83 \times 48$ taken from the same subject but at different periods. The parameters (λ, μ, τ) were set to be $(.05, .1, .004)$. The registration was performed in 3D, but for demonstration, we only show the corresponding axial (xy plane with $z = 33$), sagittal (yz plane with $x = 25$) and coronal (zx plane with $y = 48$) slices. The registration results are plotted in Fig. 5, 6 and 7, respectively. In each figure, the images in the upper row are S and T, respectively, and the images in the middle row are deformed T and S, i.e. $T(x + \bar{v})$ and $S(x + \bar{u})$, respectively. The bottom row shows the residual images $|S(x+\bar{u})-T|$, $|S-T|$ and $|T(x+\bar{v})-S|$. The mean of $CC(S(x + \bar{u}), T)$ and $CC(T(x + \bar{v}), S)$ reached .998 after 50 iterations, and the mean of inverse consistency errors was .015. The results shows the high accuracy of proposed model (18) and the well preserved inverse consistency.

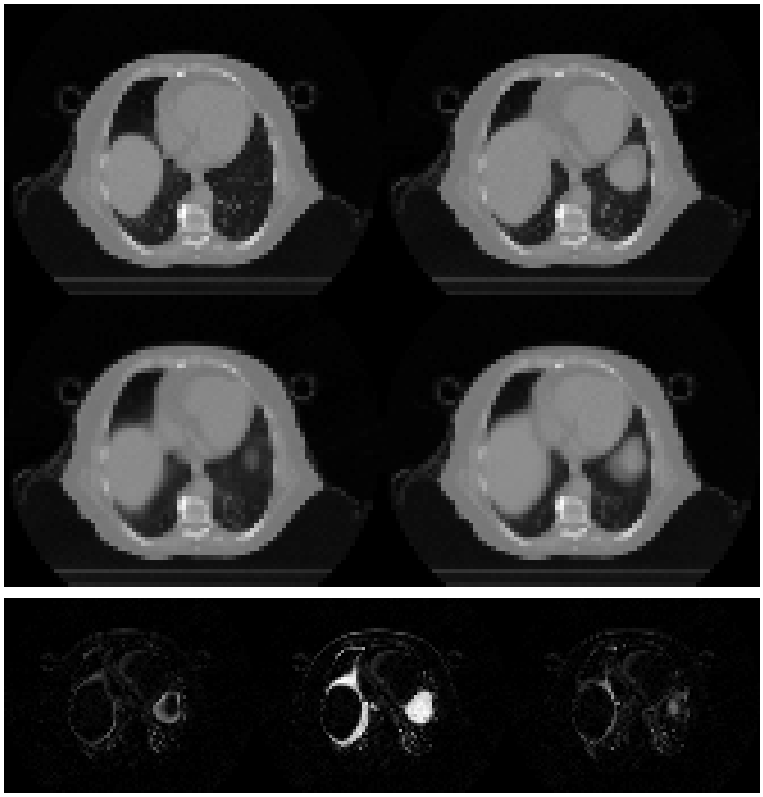

FIGURE 5. Registration result of proposed model (18) applied to 3D chest CT image. This figure shows the $z = 33$ slice at axial direction. Upper left: S. Upper right: T, Middle left: deformed T, i.e. $T(x + \bar{v})$. Middle right: deformed S, i.e. $S(x + \bar{u})$. Bottom left: residue image $|S(x + \bar{u}) - T|$. Bottom middle: initial residue image $|S - T|$. Bottom right: residue image $|T(x + \bar{v}) - S|$.

The third experiment was aimed to compare the effectiveness of model (18) with the following conventional full-way inverse consistent deformable registration model:

$$\min_{u,v,\sigma_u,\sigma_v} \|Du\|^2 + \|Dv\|^2 + \lambda J(u, v, \sigma_u, \sigma_v) + \mu \left(\mathcal{I}_v(u) + \mathcal{I}_u(v)\right) \tag{39}$$

where u and v are forward and backward deformation fields, respectively, and the term J is defined by

$$J(u, v, \sigma_u, \sigma_v) = \|S(x + u) - T\|^2/2\sigma_u^2 + \|T(x + v) - S\|^2/2\sigma_v^2 + |\Omega| \log \sigma_v \sigma_v.$$

The comparison is made on the efficiency and accuracy of matching, as well as the preservation of inverse consistency. The accuracy of matching is measured by correlation coefficients (CC) between the target image and deformed source image with the optimal forward and backward deformations obtained by model (39) and proposed model (18), respectively. Recall that for any two images S and T both

TABLE 1. Number of iterations used for convergence and the final CC obtained by proposed model with σ updated/fixed. For a large range of λ, updating σ in each iteration consistently leads to faster convergence and higher accuracy.

	Update σ		Fix σ	
λ	CC	Iter	CC	Iter
1e2	.962	48	.955	89
1e1	.962	97	.946	420
1e0	.960	356	.933	1762

with N pixels, the CC of S and T is defined by

$$CC(S,T) = \frac{\sum_{i=1}^{N}(S_i - \bar{S})(T_i - \bar{T})}{\sqrt{\sum_{i=1}^{N}(S_i - \bar{S})^2 \sum_{i=1}^{N}(T_i - \bar{T})^2}},$$

where S_i and T_i are the intensities at the ith pixels of S and T, respectively, $\bar{S}$ and $\bar{T}$ are the mean intensities of S and T, respectively. The maximum value of CC is 1, in which case S and T are (positively) linearly related. In this experiment we applied models (39) and (18) to the images in the first experiment shown in Fig. 1 with the same parameters (λ, μ, τ) to be $(.05, .2, .05)$. In Fig. 5, we plotted the CC obtained by model (39) and proposed model (18) at each iteration. One can observed that the CC obtained by model (18) is higher and increases faster than model (39). This demonstrates that proposed model (18) is more efficient than the conventional full-way model. The reason is that the disparity between deformed S and deformed T is smaller than that between deformed S and fixed T or deformed T and fixed S. When S and T are deformed simultaneously, the two directional deformation fields are not necessarily to be large even if the underlying deformation field is large, which usually makes it difficult for the full-way based registration model to reach a satisfactory alignment in short time.

The last experiment is aim to test the robustness of the model to noises and the choice of the parameter λ with the use of MLE based approach (11) for measuring the goodness of matching. The images S and T in Fig. 1 with additive Gaussian noises (standard deviation is 3% of largest intensity value of S) were used in this experiment. The CC between S and T before registration is $CC(S,T) = .901$. We applied model (18) with σ to be updated/optimized by its EL equation (35), and σ to be set $\sigma = 1$, that is the same as using SSD as similarity measure, respectively, to the noise data mentioned above. We proceeded the registration with various values of λ, but kept other parameters fixed. Then the numbers of iterations (Iter) for convergence and the final CC were recorded and shown in Table 1. One can see that while λ decreases, the accuracy of model (18) using fixed σ reduces as the final CC become much smaller, and it also takes much longer time for the algorithm to converge. On the other hand, with σ being updated (whose computational cost is extremely cheap) model (18) can obtain good matching in much less iterations for a large range of λ. This shows that model with MLE fitting is much less sensitive to noise and the choice of λ, and can achieve fast and accurate results compared with the model using SSD to measure mismatching.

References

[ADPS02] L. Alvarez, R. Deriche, T. Papadopoulo, and J. Sanchez, *Symmetrical dense optical flow estimation with occlusions detection*, Proceedings of European Conference on Computer Vision (2002), 721–735.

[AGG06] B. B. Avants, M. Grossman, and J. C. Gee, *Symmetric diffeomorphic image registration: Evaluating automated labeling of elderly and neurodegenerative cortex and frontal lobe*, Proceedings of Biomedical Image Registration **4057** (2006), 50–57.

[BK07] Mirza Faisal Beg and Ali Khan, *Symmetric data attachment terms for large deformation image registration*, IEEE Transactions on Medical Imaging **26** (2007), no. 9, 1179–1189.

[CJ01] G. E. Christensen and H. J. Johnson, *Consistent image registration*, IEEE Transactions on Medical Imaging **20** (2001), no. 7, 721–735.

[HC03] J. C. He and G. E. Christensen, *Large deformation inverse consistent elastic image registration*, Proceedings of Information Processing in Medical Imaging **2732** (2003), 438–449.

[JDJG04] S. Joshiand, B. Davis, M. Jomier, and G. Gerig, *Unbiased diffeomorphic atlas construction for computational anatomy*, Neuroimage, Supplement **23** (2004), no. 1, 151–160.

[Kes06] M. L. Kessler, *Image registration and data fusion in radiation therapy*, British Journal on Radiology **79** (2006), 99–108.

[LHG+05] A.D. Leow, S.C. Huang, A. Geng, J. Becker, S. Davis, A. Toga, and P. Thompson, *Inverse consistent mapping in 3d deformable image registration: its construction and statistical properties*, Proceedings of Information Processing in Medical Imaging (2005), 493–503.

[LOC+06] W. Lu, G. H. Olivera, Q. Chen, M. Chen, and K. Ruchala, *Automatic re-contouring in 4d radiotherapy*, Physics in Medicine and Biology **51** (2006), 1077–1099.

[RK06] P. Rogelj and S. Kovacic, *Symmetric image registration*, Medical Image Analysis **10** (2006), no. 3, 484–494.

[WtHRV98] Joachim Weickert, Bart M. ter Haar Romeny, and Max A. Viergever, *Efficient and reliable schemes for nonlinear diffusion filtering*, IEEE Transactions on Image Processing **7** (1998), no. 3, 398–410.

[YS05] S.K. Yeung and P.C. Shi, *Stochastic inverse consistency in medical image registration*, International Conference on Medical Image Computing and Computer-Assisted Intervention **8** (2005), no. 2, 188–196.

[YTS+08] Sai-Kit Yeung, Chi-Keung Tang, Pengcheng Shi, Josien P.W. Pluim, Max A. Viergever, Albert C.S. Chung, and Helen C. Shen, *Enforcing stochastic inverse consistency in non-rigid image registration and matching*, Proceedings of IEEE Conference on Computer Vision and Pattern Recognition (2008), 1–8.

[ZC08] Q. Zeng and Y. Chen, *Accurate inverse consistent non-rigid image registration and its application on automatic re-contouring*, Proceedings of International Symposium on Bioinformatics Research and Applications (2008), 293–304.

[ZJT06] Z. Zhang, Y. Jiang, and H. Tsui, *Consistent multi-modal non-rigid registration based on a variational approach*, Pattern Recognition Letters (2006), 715–725.

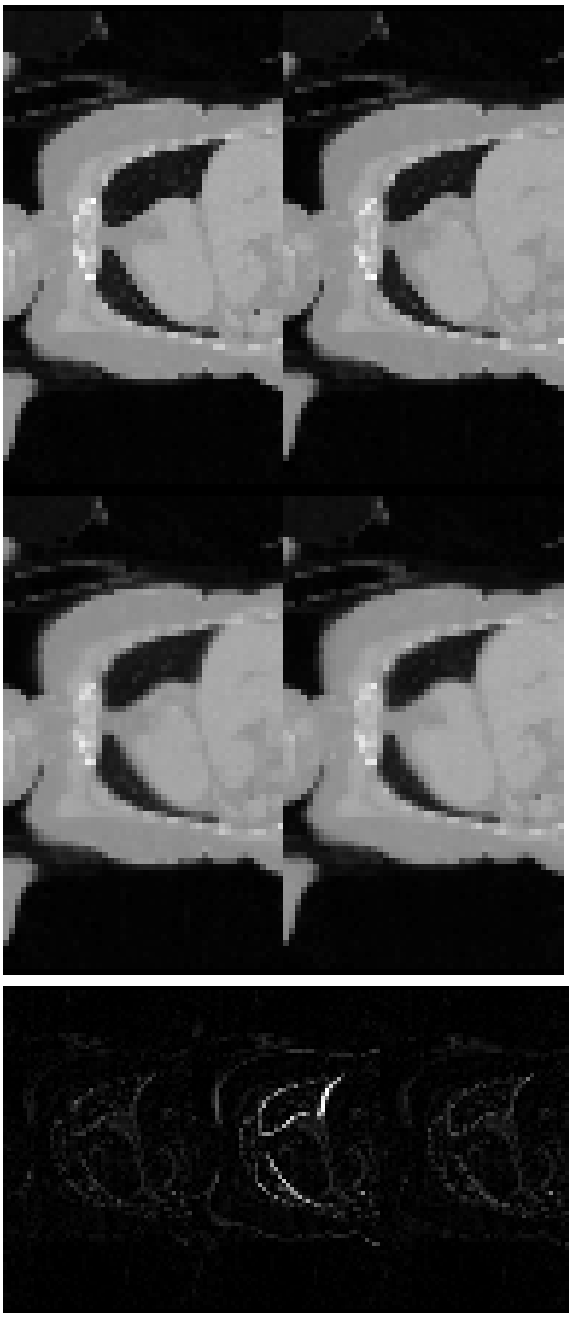

FIGURE 6. Registration result of proposed model (18) applied to 3D chest CT image. This figure shows the $x = 25$ slice at sagittal direction. Upper left: S. Upper right: T, Middle left: deformed T, i.e. $T(x + \bar{v})$. Middle right: deformed S, i.e. $S(x + \bar{u})$. Bottom left: residue image $|S(x + \bar{u}) - T|$. Bottom middle: initial residue image $|S - T|$. Bottom right: residue image $|T(x + \bar{v}) - S|$.

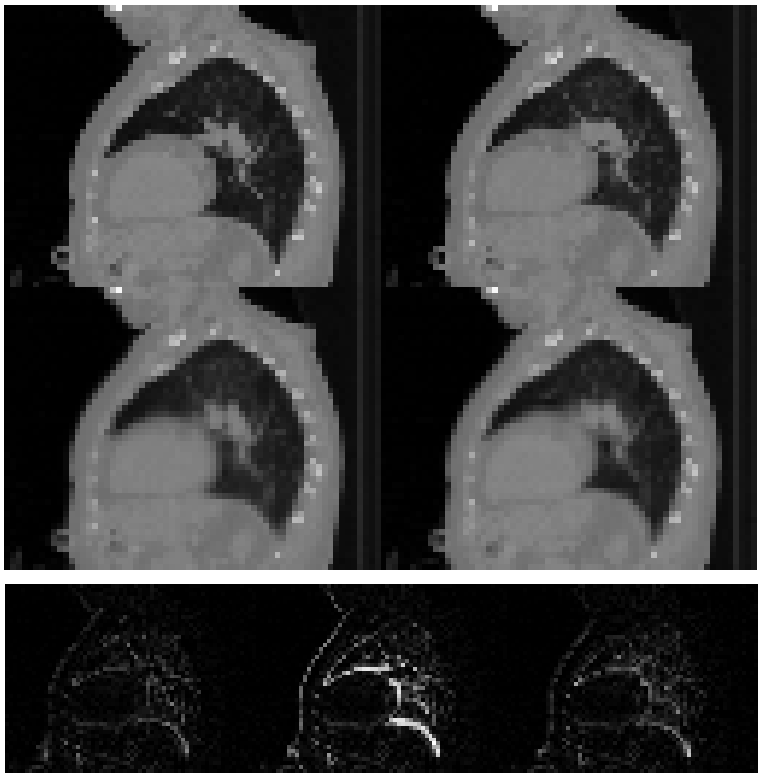

FIGURE 7. Registration result of proposed model (18) applied to 3D chest CT image. This figure shows the $y = 48$ slice at coronary direction. Upper left: S. Upper right: T, Middle left: deformed T, i.e. $T(x + \bar{v})$. Middle right: deformed S, i.e. $S(x + \bar{u})$. Bottom left: residue image $|S(x + \bar{u}) - T|$. Bottom middle: initial residue image $|S - T|$. Bottom right: residue image $|T(x + \bar{v}) - S|$.

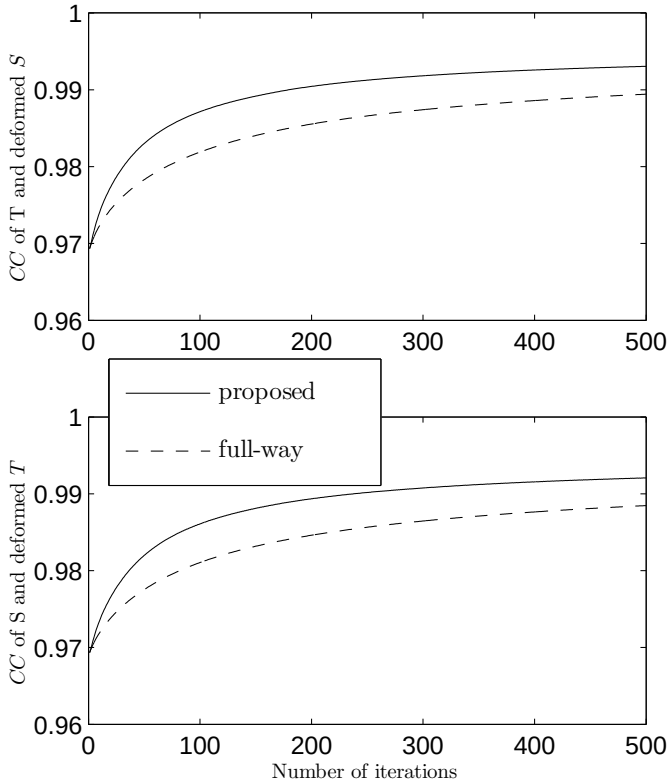

FIGURE 8. CC in each iteration obtained by full-way model (39) and proposed model (18). Proposed model (18) gives quick matching with better accuracy, as CC by model (18) increase much faster and can reach higher limits than that by full-way model (39).

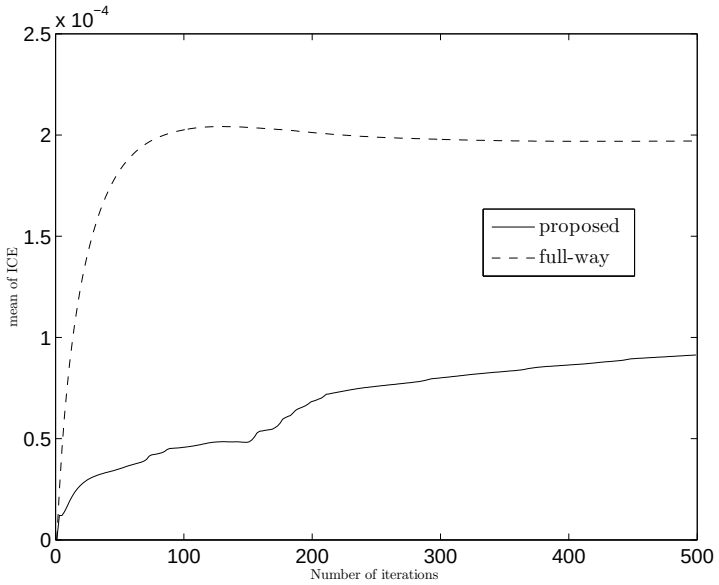

FIGURE 9. Mean of inverse consistent errors (ICE) of the final deformation fields obtained by using full-way model (39) and proposed model (18). The value is much smaller than the size of grid between concatenate pixels, which shows that the inverse consistency is preserved.